

Valley switch effect in an α-T_3 lattice-based superconducting interferometer

Ya-Jun Wei(魏亚军) and Jun Wang(汪军)

Citation: Chin. Phys. B, 2024, 33 (**11**): 117201. DOI: 10.1088/1674-1056/ad6f91
Journal homepage: http://cpb.iphy.ac.cn; http://iopscience.iop.org/cpb

What follows is a list of articles you may be interested in

Valley filtering and valley-polarized collective modes in bulk graphene monolayers

Jian-Long Zheng(郑建龙) and Feng Zhai(翟峰)
Chin. Phys. B, 2024, 33 (**1**): 017203. DOI: 10.1088/1674-1056/acfd17

Valley polarization in transition metal dichalcogenide layered semiconductors: Generation, relaxation, manipulation and transport

Hui Ma(马惠), Yaojie Zhu(朱耀杰), Yulun Liu(刘宇伦), Ruixue Bai(白瑞雪), Xilin Zhang(张喜林), Yanbo Ren(任琰博), and Chongyun Jiang(蒋崇云)
Chin. Phys. B, 2023, 32 (**10**): 107201. DOI: 10.1088/1674-1056/ace160

Influence of Rashba spin-orbit coupling on Josephson effect in triplet superconductor/two-dimensional semiconductor/triplet superconductor junctions

Bin-Hao Du(杜彬豪), Man-Ni Chen(陈嫚妮), and Liang-Bin Hu(胡梁宾)
Chin. Phys. B, 2022, 31 (**7**): 077201. DOI: 10.1088/1674-1056/ac587e

Current induced nonequilibrium spin polarization in semiconductor-nanowire/s-wave superconductor junctions with strong spin-orbit coupling

Nai-Qing Liu(刘乃清), Li-Jie Huang(黄立捷), Rui-Qiang Wang(王瑞强), Liang-Bin Hu(胡梁宾)
Chin. Phys. B, 2016, 25 (**2**): 027201. DOI: 10.1088/1674-1056/25/2/027201

Spin and valley filter in strain engineered silicene

Wang Sa-Ke (汪萨克), Wang Jun (汪军)
Chin. Phys. B, 2015, 24 (**3**): 037202. DOI: 10.1088/1674-1056/24/3/037202

Valley switch effect in an α-T_3 lattice-based superconducting interferometer

Ya-Jun Wei(魏亚军) and Jun Wang(汪军)†

School of Physics, Southeast University, Nanjing 210096, *China*

(Received 13 May 2024; revised manuscript received 3 August 2024; accepted manuscript online 15 August 2024)

Dirac electrons possess a valley degree of freedom, which is currently under investigation as a potential information carrier. We propose an approach to generate and manipulate the valley-switching current (VSC) through Andreev reflection using an interferometer-based superconductor hybrid junction. The interferometer comprises a ring-shaped structure formed by topological kink states in the α-T_3 lattice via carefully designed electrostatic potentials. Our results demonstrate the feasibility of achieving a fully polarized VSC in this device without contamination from cotunneling electrons sharing the same valley as the incident electron. Furthermore, we show that control over the fully polarized VSC can be achieved by applying a nonlocal gate voltage or modifying the global parameter α. The former alters the dynamic phase of electrons while the latter provides an α-dependent Berry phase, both directly influencing quantum interference and thereby affecting performance in terms of generating and manipulating VSC, crucial for advancements in valleytronics.

Keywords: valley switch effect, valleytronics, Andreev reflection, α-T_3 lattice

PACS: 72.15.–v, 72.90.+y, 73.20.–r, 73.23.–b **DOI:** 10.1088/1674-1056/ad6f91

1. Introduction

There is a phase-coherent scattering process known as Andreev reflection (AR) in the superconducting heterojunction:[1–4] an incident electron from the normal conductor can be reflected as a hole at the interface between a superconductor (S) and a normal conductor. The AR also provides a mechanism that the electrons can transport in the superconducting energy gap. Additionally, as Dirac electrons possess a valley degree of freedom, the occurrence of Andreev reflection at the interface between a superconductor and a Dirac material results in the occupation of distinct valleys by the Andreev reflected hole and incident electron.[3–5]

Numerous studies have been dedicated to investigating the valley switch effect due to its remarkable properties and potential applications in valleytronics.[3–11] For example, Beenakker conducted research on electron–hole conversion at a normal metal–superconductor interface in graphene.[4] They found that the valley switching AR could either exhibit retroreflection or specular reflection. Recently, Beenakker also investigated valley switch effect in a graphene superlattice through pseudo-Andreev reflection.[11] They demonstrated that a superlattice potential can induce valley switch: when electrons approach a pristine graphene–superlattice graphene interface at near-normal incidence, they undergo reflection into the opposite valley. Moreover, the valley switch is maximized at a symmetry point of the superlattice potential and remains close to 100% within a wide parameter range.

Experimental evidence[12–22] confirms the presence of one-dimensional valley–momentum locking topological kink states in graphene systems with spatial inversion symmetry broken, which can be easily designed via staggered potentials by using external electric fields. These kink states are localized near a domain wall (or line in the 2D graphene sheet) and exhibit similar characteristics to helical spin states, allowing for the flow of two opposite valleys in opposite directions along the domain wall. The kink state similar to the spin helical state allows pump of Cooper pairs because the singlet Cooper pairs involve two electrons with opposite valleys (momenta). Consequently, it is plausible to design a quantum interferometer based on the topological kink states to manipulate the valley switch effect.

The α-T_3 lattice is an interpolate between the graphene and dice lattices[23] and the hopping of electrons between the hub atom at each hexagon of the honeycomb lattice and neighboring atoms can be modulated by α, and more importantly, the Dirac electrons of the system have an α-dependent nonquantized Berry phase, $\gamma = \pm\pi(1-\alpha^2)/(1+\alpha^2)$ for the K (K') valley,[24] which should affect the related electron transport properties. Several methods have been proposed to realize the α-T_3 lattice in experiments.[25–28] For example, the dice lattice with $\alpha = 1$ can be produced in $SrTiO_3$/$SrIrO_3$/$SrTiO_3$ trilayer heterostructure grown along the (111) direction.[25] The multilayer structure of the α-T_3 lattice as the same as the bilayer graphene is quite suitable for the possible kink states formed via perpendicular electric fields.[22]

In this work, we devise a four-terminal α-T_3-based interferometer with a superconductor covering one lead to manipulate the valley switching AR, where the interferometer is devised as a ring-shaped kink states through special arrangement of the perpendicular electric fields. Our findings demon-

†Corresponding author. E-mail: jwang@seu.edu.cn

© 2024 Chinese Physical Society and IOP Publishing Ltd

strate that the AR process in this device not only enables valley switching but also facilitates fully polarized valley switching current (VSC) without any elastic cotunneling in the interferometer. This behavior can be controlled either by adjusting a nonlocal gate voltage or by tuning the system parameter α, thanks to quantum interference effects. Moreover, we reveal that the α-dependent Berry phase γ of electrons plays a crucial role in determining oscillations of the VSC.

This work is organized as follows: In Section 2, we present a model of superconductor hybrid junction based on the kink states in the α-T_3 lattice, and the calculation method is also introduced. In Section 3, the numerical results of the manipulation of valley switch effect as well as some discussions are presented. A brief conclusion is finally given in Section 4.

2. Model

We start from the α-T_3 lattice structure as schematically shown in Fig. 1(a), where the AB atoms construct the graphene lattice while a hub C atom resides in each hexagon center. The parameter α is manifested in the hopping energy between the sites B and C, $t' = \alpha t$, where t is the hopping energy between the A and B sites of the graphene lattice, the hopping between the A and C sites is prohibited. Hence, $\alpha = 0$ represents the graphene lattice while $\alpha = 1$ denotes the Dice one. The α-T_3 lattice Hamiltonian reads

$$H_0 = \sum_{i\sigma} V_i c^{\dagger}_{i\sigma} c_{i\sigma} + \sum_{\langle ij\rangle,\sigma} t c^{\dagger}_{i\sigma} c_{j\sigma} + \sum_{\langle jk\rangle,\sigma} t' c^{\dagger}_{j\sigma} c_{k\sigma}, \quad (1)$$

where $c^{\dagger}_i$ and c_i are the creation and annihilation operators of electrons at site i, respectively; σ is the spin index and V_i indicates the on-site energy which can be used to define a domain wall to form the topological kink state. The second term is the electron hopping between the A and B sites while the third one is between the B and C sites. The summation of $\langle ij\rangle$ ($\langle jk\rangle$) runs over the nearest neighbor sites of AB (BC). By solving Eq. (1) in the bulk of the lattice under a periodic boundary condition along x- and y-axes, one can obtain the bulk energy spectrum in Fig. 1(b), where a flat band sits at the band center across the two Dirac cones in K and K' valleys.

As is known, the topological kink state or interface state would form to connect the neighboring two topologically different insulating regions. Take graphene as an example, it becomes a quantum valley Hall insulator when a staggered potential is applied to the system, as a result, the valley helical state (kink state) could appear if the neighboring regions have the opposite topological invariants, i.e., the K valley and K' valley electrons flow in the opposite directions with a definite chirality. The kink state has been observed in the bilayer graphene system, since the perpendicular electric fields can lead to the staggered potential opening an energy gap, and the domain wall is easy to be realized.[14]

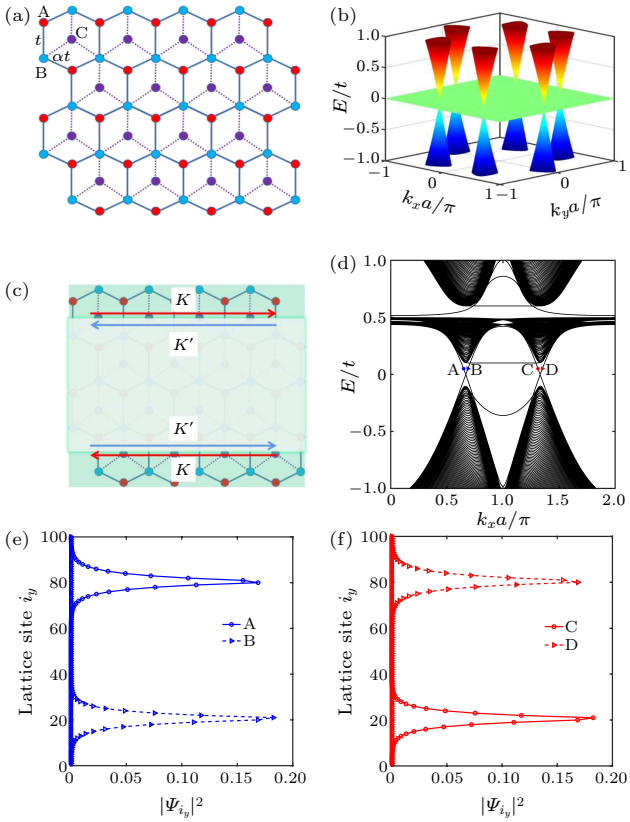


Fig. 1. (a) Schematic of the α-T_3 lattice structure, where A and B sites constitute the honeycomb lattice while the C site resides in each hexagon center. (b) Bulk energy spectrum in the α-T_3 lattice for $V_i = \alpha = \varepsilon = 0$. A flat band sits at the crossing point of the two Dirac cones. (c) Schematic view of the sandwiched α-T_3 nanoribbon, where the domain walls are defined by the interface of cyan and grey regions in which the sign of staggered potential reverses. (d) Electronic band structures of the sandwiched α-T_3 nanoribbon with topological kink states. Wave-function distributions (Ψ_{i_y}) of the interface states marked in (d) on the transverse ribbon site i_y for K' and K valleys in (e) and (f). Parameters are $\alpha = 0.5$, $\varepsilon = 0.6t$, $U = 0.1t$, and the number of unit cell $N_y = 100$.

The α-T_3 is also a layer structure, so it is not difficult to obtain the topological kink states by devising a domain wall via simple perpendicular electric fields, i.e., $V_A = V_g + (-)U$, $V_B = V_g - (+)U$ and $V_C = V_g + \varepsilon$ for the cyan (gray) region in Fig. 1(c). The energy band of the sandwich-shaped α-T_3 nanoribbon with different staggered potentials is presented in Fig. 1(d) for the case of $\alpha = 0.5$, where the open boundary condition along the y-axis and a periodic boundary condition along the x-axis are considered. There are two helical interface states in the band gap referred to as the topological kink states, while the flat band is excluded from the band gap by setting $\varepsilon = 0.6$ to avoid complicating the kink states because it can now exhibit a dispersion with the applied staggered potential V_A/V_B. The wave-function distribution for the marked points in the energy band is plotted for K' valley in Fig. 1(e) and for K valley in Fig. 1(f). The finite size of the ribbon is set as $N_y = 100$ denoting the finite number of the transverse zigzag atom chain. The K and K' valley chiralities are labeled

in Fig. 1(c). Moreover, the electrons in the α-T_3 lattice have an α-dependent Berry phase, $\gamma = \pm\pi(1-\alpha^2)/(1+\alpha^2)$ for the K (K') valley, which can provide an extra method to manipulate the electron transport.

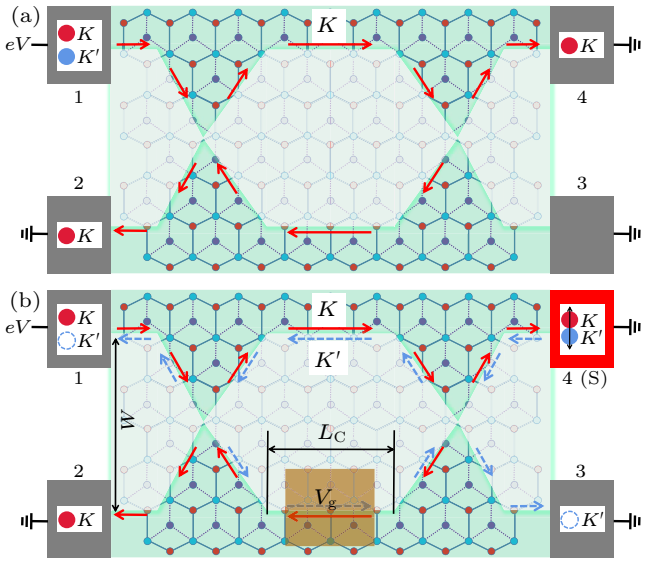


Fig. 2. Schematic view of the four-terminal interferometer composed of topological kink states by the domain walls (a). (b) Superconducting heterojunction based on the interferometer with a superconductor covering the terminal 4, where S indicates superconductor, W denotes the distance between terminals 1 and 2, L_C is the length of the parallel segment of the interferometer, and V_g is a gate voltage applied onto the lower kink state region.

One can devise a four-terminal interferometer based on the α-T_3 lattice by using the kink states composed of domain walls as shown in Fig. 2(a). The middle part of the device is a ring-shaped conducting circuit and it has been used to discern the Berry phase of electrons in both the monolayer and bilayer graphene.[22] When a small bias is applied onto one of terminals, say terminal 1, while the other terminals are grounded, only electrons of the K valley can flow out from terminal 1 into the central region. The incoming electron waves from terminal 1 at the left crossed point are partitioned to terminal 2 and the upper arm of the interferometer. At the right crossed point of the ring-like structure, the waves are split into terminal 4 and the lower arm of the circuit. Then the partial waves along the lower arm travel back to the left cross point and are split for the third time. The process shall occur repeatedly in the whole circuit and the current flowing into terminals 2, 3, and terminal 4 shall necessarily include the quantum interference effect. The red solid arrow denotes the circulating of the K electrons in the device injected from terminal 1 in Fig. 2(a).

Based on the above device, we now consider a superconductor electrode put onto the terminal 4 in Fig. 2(b). The superconductivity in the lattice is assumed from the superconducting proximity effect, which is expressed as[3,4,29,30]

$$H_{\rm S} = \sum_{i\sigma} \Delta \cdot c^{\dagger}_{i\sigma} c^{\dagger}_{i\bar{\sigma}} + {\rm c.c.}, \tag{2}$$

where $\sigma = -\bar{\sigma}$ is the spin indices and Δ denotes the pair potential. The uniform pair potential is taken into account on each site, and here, the self-consistent calculations of the pair potential are neglected. However, the qualitative results shall remain unchanged because for one thing, the s-wave superconductivity is adopted and no special pair symmetry is required, and for the other thing, the pair potential strength is too weak in comparison with other interaction strength. When the K-valley electrons from the biased terminal 1 reach the superconducting lead (terminal 4), the reflected K'-valley hole denoted by dashed arrows in Fig. 2(b) would travel along the interferometer and either return to terminal 1 or terminal 3, the former is termed as the local VSC but the latter can be called nonlocal VSC.

In order to investigate the VSC in the above superconducting hybrid junction of Fig. 2(b), we adopt the transfer matrix method and obtain the scattering matrix by using the Fisher–Lee relation[30,31]

$$S^{p,q}_{m,n} = -\delta_{m,n}\delta_{p,q} + {\rm i}[\Gamma^{p}_{m}]^{\frac{1}{2}} G^{p,q}_{m,n} [\Gamma^{q}_{n}]^{\frac{1}{2}}, \tag{3}$$

where $p,q \in \{{\rm e},{\rm h}\}$ label the electron or hole and $m,n \in \{1,2,3,{\rm S}\}$ represent the four terminals. The matrix $S^{p,q}_{m,n}$ denotes the scattering amplitude of the process where an incident particle p from terminal m is scattered into a particle q in terminal n. $\Gamma^{p(q)}_{m(n)}$ is a block of the linewidth function $\Gamma_{m(n)} = {\rm i}[\Sigma^{\rm r}_{m(n)} - \Sigma^{\rm a}_{m(n)}]$ with retarded/advanced self-energy $\Sigma^{\rm r/a}_{m(n)}$ due to the coupling to the lead $m(n)$ which can be calculated numerically by the recursive method. $G^{p,q}_{m,n}$ is the matrix block of the retarded Green's function of the interferometer in the Nambu space, which is determined by $G^{\rm r} = [E - H'_0 - \Sigma^{\rm r}]^{-1}$. $H'_0 = H_0 + H_{\rm S}$ is the scattering-region Hamiltonian of the ribbon device in Fig. 2(b), while the left and right parts of the ribbon are assumed to be semi-infinite long and denoted by the lead self energy $\Sigma^{\rm r} = \Sigma^{\rm r}_1 + \Sigma^{\rm r}_2 + \Sigma^{\rm r}_3 + \Sigma^{\rm r}_{\rm S}$. All matrices are considered in the Nambu space. The AR coefficient $R^{\rm e,h}_{m,n}$ can be calculated by $R^{\rm e,h}_{m,n} = {\rm Tr}\{[S^{\rm e,h}_{m,n}]^{\dagger} S^{\rm e,h}_{m,n}\} = {\rm Tr}\{\Gamma^{\rm h}_{n} G^{\rm e,h}_{m,n} \Gamma^{\rm e}_{m} [G^{\rm e,h}_{m,n}]^{\dagger}\}$. The other scattering coefficients $T^{p,q}_{m,n}$ can also be worked out in the same way.

3. Results and discussion

In the numerical calculation, we use $U = 0.1t$, $\varepsilon = 0.6t$, and $\Delta = 0.005t$ with $t = 1$ as the energy unit in Eq. (1). The ring-structured interferometer is simplified by a hexagon for easy calculation in practice, which has no virtual effect on the results due to the topology of the kink states. At zero temperature limit, the current $I_{m,n}$ is proportional to $T_{m,n}$ due to the Landauer–Buttiker formula, so we only concern $R_{m,n}$ and $T_{m,n}$ in the following discussion. The superconducting coherence length $\xi = \hbar v_F/\Delta \sim 876a/\cos\theta$ with $\tan(2\theta) = \alpha$ and a, the lattice constant. Note that only the terminal 1 is biased while

the other terminals are grounded. In addition, there is a gate voltage set on the circuit but not on the line between terminals 3 and 4.

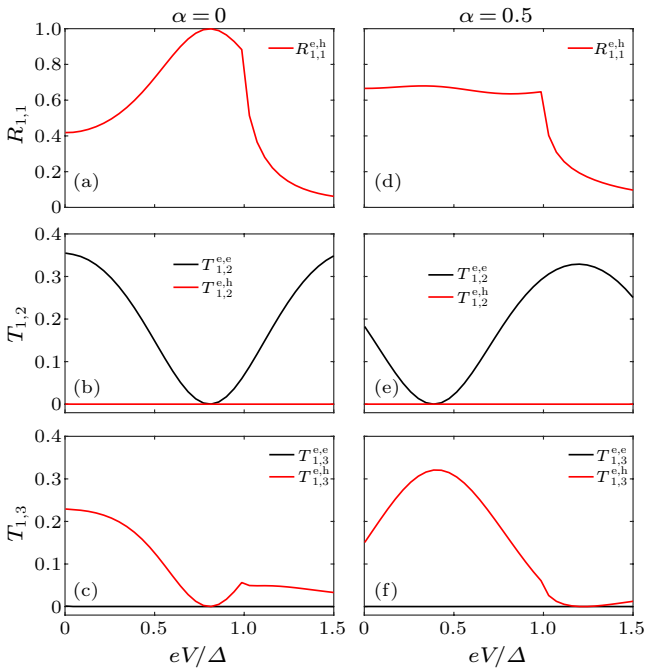


Fig. 3. Bias voltages eV dependence of $R_{1,1}$ [(a), (d)], $T_{1,2}$ [(b), (e)], $T_{1,3}$ [(c), (f)] for $\alpha = 0$ and 0.5. Parameters are $L_C = 4W$ with $W = 60\sqrt{3}a$, $\Delta = 0.005t$, and the other parameter are chosen as those in Fig. 1(d).

The scattering coefficients versus the bias voltage eV is plotted in Fig. 3 including the local VSC ($R^{e,h}_{1,1}$) of terminal 1, normal electron transmission ($T^{e,e}_{1,2}$) and nonlocal VSC ($T^{e,h}_{1,2}$) of terminal 2, normal electron transmission ($T^{e,e}_{1,3}$), and nonlocal VSC $T^{e,h}_{1,3}$ of terminal 3. The left panel is for $\alpha = 0$ while the right one is for $\alpha = 0.5$. It is clear that the nonlocal VSC $T^{e,h}_{1,2} = 0$ in terminal 2 and transmission $T^{e,e}_{1,3} = 0$ in terminal 3 for the K valley electrons incident from terminal 1. $T^{e,h}_{1,3} \neq 0$ and $T^{e,e}_{1,3} = 0$ denote the fully polarized VSC occurring in terminal 3 without electron cotunneling. The results are in accordance with the aforementioned analysis, and the physics can be attributed to the inherent chirality of the topological kink states.

The process is that only the K-valley electrons can flow out from terminal 1 under a small voltage bias and then are partitioned repetitively at the left and right crossing points of the ring-structured interferometer in Fig. 2(b). Only these electrons fulfilling the local chirality of the kink state can tunnel out the corresponding terminal. Thus, there is no K valley electron flowing into terminal 3 $T^{e,e}_{1,3} = 0$ but only K' valley hole is feasible due to the nonlocal VSC process in the device, which is fully polarized VSC. Similarly, there is no K'-valley electron or hole flowing into terminal 2 with $T^{e,h}_{1,2} = 0$. Certainly, the K'-valley hole, which exhibits electron chirality in the kink states, can also be reflected into terminal 1. As a result, local VSC occurs with $T^{eh}_{11} \neq 0$, indicating a mixed current contribution from both K and K' valleys.

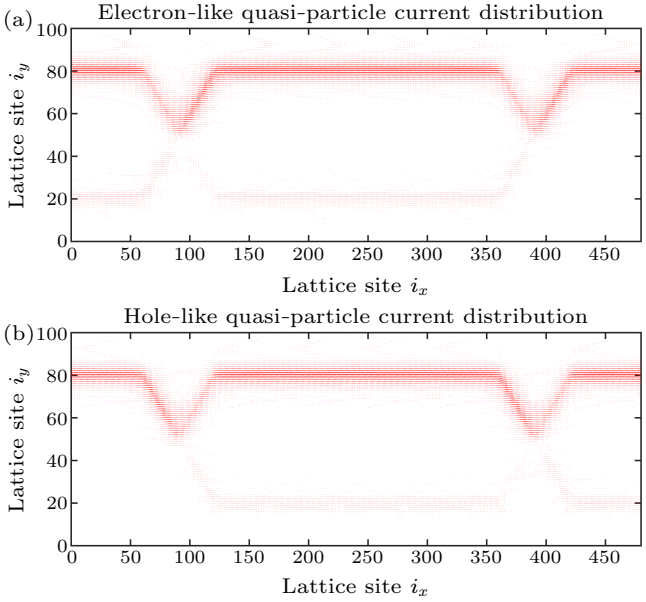


Fig. 4. Current distribution for electron-like (a) and hole-like (b) quasiparticles with $\alpha = 0.5$ and $eV = 0.1\Delta$. The other parameters are chosen as those in Fig. 3.

In Fig. 4(a), the electron-like quasiparticle current distribution in real (lattice) space is presented by calculating the nonequilibrium current density.[32,33] It is important to see that there is no electron-like current flowing in terminal 3, while the current density is nonzero in terminal 2. This is consistent with the above analysis. The hole-like current density distribution is also plotted in Fig. 4(b), and one can see that the Andreev reflected hole from K' valley would travel alone ring-like circuit and flow into terminal 1 and 3 but terminal 2 forbidden, $T^{e,h}_{1,2} = 0$. Correspondingly, the nonlocal VSC $T^{e,h}_{1,3}$ can be obtained without mixture of elastic cotunneling $T^{e,e}_{1,3} = 0$ in terminal 3. Moreover, the current flowing in terminal 3 is only the K' valley so it is fully valley polarized. It is seen that the summation of scattering coefficients of local VSC $R^{e,h}_{1,1}$, transmission $T^{e,e}_{1,2}$, and nonlocal VSC $T^{e,h}_{1,3}$ is nearly equal to a unit 1, i.e., $R^{e,h}_{1,1} + T^{e,e}_{1,2} + T^{e,h}_{1,3} \simeq 1$, the difference is just a numerical system error.

It is also shown in Fig. 3 that the probability of local VSC reaches the maximum, $R^{e,h}_{1,1} = 1$, at $eV \simeq 0.8\Delta$ for $\alpha = 0$, where both the permitted transmission $T^{e,e}_{1,2}$ and nonlocal VSC $T^{e,h}_{1,3}$ vanish. It can be attributed to the phase resonant effect of electron and hole in the ring-structured interferometer, as discussed in Ref. [22]. In detail, the incoming wave of K-valley from terminal 1, at left crossing point, is partitioned to terminal 2 and upper arm of the interferometer. At the right crossing point, again the wave of K valley is split to terminal 4 and the lower arm. Then the wave along the lower arm meets the first crossing point and is split for the third time. The process happens repeatedly and the current flow into terminal 2 or reach terminal 4, resulted from the multibeam interference. When the wave travel along the interferometer, it would gain dynamic phase and Berry phase. For waves of K valley reaching

terminal 4 with phase difference $2n\pi$, they would phase resonate to a maximum. Then the K-valley electrons is reflected as K' valley holes through AR at the interface between the interferometer and superconduct lead. Subsequently, the reflected K' valley holes would also exhibit maximum resonance in terminal 1, owing to their synchronization with the phase of the initial K-valley electrons; while for $\alpha = 0.5$, this phenomenon disappears as seen in the right column of Fig. 3. It occurs because of the inequality of dynamic phase for the electron and Andreev reflected hole in the interferometer caused by the energy band of the kink state modified due to nonzero α.

Since the outgoing wavefunctions are strongly dependent on the quantum interference effect, one can in principle modulate the transmission or reflection coefficient in each terminal. The nonlocal VSC, $T^{e,h}_{1,3}$, as a function of the gate voltage V_g for various α, is plotted in Fig. 5. Clearly, $T^{e,h}_{1,3}$ shows an oscillating behavior and it can even be totally suppressed, $T^{e,h}_{1,3} = 0$ due to the destructive resonant effect. The gate voltage has the ability to modify the local Fermi level, thereby influencing the momentum of quasiparticles traveling along the lower arm of the interferometer [Fig. 2(b)] and subsequently altering their dynamic phase accumulated in this path. This holds significant implications for the quantum interference effects. Note that the nonlocal VSC denotes the current magnitude between terminals 3 and 4 while the gate voltage V_g is not applied onto the local circuit, the controllable nonlocal VSC here is significant because it can be controlled in a remote way without interference.

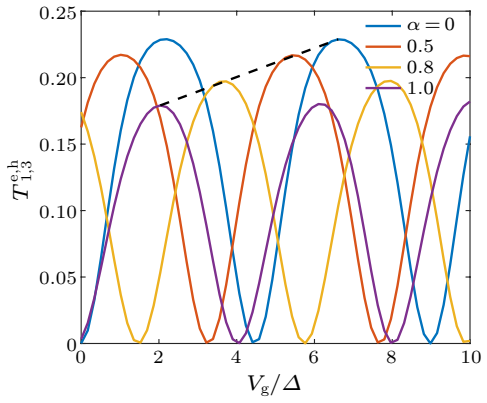


Fig. 5. Nonlocal VSC $T^{e,h}_{1,3}$ versus the gate voltage V_g for different α. Parameters are $eV = 0.8\Delta$ and the others are the same as those in Fig. 3.

In addition, it is noted that the oscillation of nonlocal VSC versus V_g in Fig. 5 is shifted with α. This occurs mainly due to the α-dependent Berry phase $\gamma = \pm\pi(1-\alpha^2)/(1+\alpha^2)$ for K (K') valley in the α-T_3 lattice. Since we design a ring-like structure of the conductive kink states, which is similar to the usual Aharonov–Bohm effect within external magnetic flux threading the ring, the scattering coefficients shall in principle reflect the dependence on α. However, the case is different from the Aharonov–Bohm effect, where the electron band structure is not modified by the magnetic flux and the Berry phase affecting the transport is independent of the concrete closed path. However, in the studied model here, the band structure of topological kink states in the designed domain wall also relies on the α-dependent Berry phase,[34] which will alter the momentum of the quasiparticles traveling along the interferometer. As a result, the dynamic phase accumulated by electrons and Andreev reflected holes will affect the interference effect and then the nonlocal VSC $T^{e,h}_{1,3}$. Therefore, the scattering coefficients depend on α in a complex way. The black dashed line labeled in Fig. 5 denotes a decreasing Berry phase since the phase shift of the nonlocal VSC oscillation gradually increases with an increase of α.

We also depict the nonlocal VSC ($T^{e,h}_{1,3}$) varying with α for different system lengths L_C in Fig. 6. It is seen that α can exert the same function as V_g, and $T^{e,h}_{1,3}$ is oscillating with α. It is mainly attributed to the α-dependent Berry phase, which acts like a magnetic flux from a magnetic field in the interferometer. The oscillating amplitude of $T^{e,h}_{1,3}$ versus α is gradually increasing with the system size L_C but without significant amplitude attenuation. Similarly, the nonlocal VSC can be entirely suppressed for certain parameters of α as the same as V_g. Notice that the dynamic phase is also varied when α alters in the system, because the velocity of electrons in the kink state is changed with α, alternatively the variation of the Berry phase will inevitably modify the energy dispersion of electrons in the ring-shaped kink state.

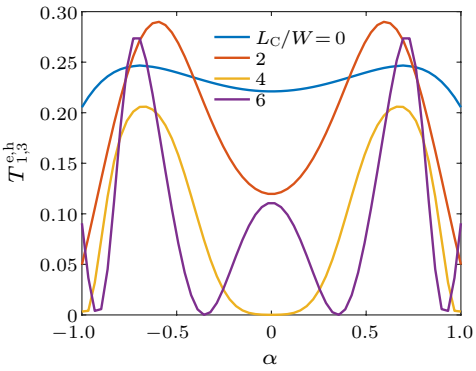


Fig. 6. Nonlocal VSC $T^{e,h}_{1,3}$ versus α for various length L_C. Parameters are $eV = 0.8\Delta$ and the others are the same as those in Fig. 3.

In the above discussion, we have shown that a fully polarized nonlocal VSC is possible in the studied device and it can be manipulated either by a gate voltage or by the system's parameter α. The former even renders a remote way to control the nonlocal VSC. The key point is the topological kink state obtained in experiments. As a matter of fact, this kink state has been observed in the bilayer graphene system[15,16] via perpendicular fields and our proposal is applicable for the bilayer graphene material as well. Nevertheless, the α-T_3 material is a layer structure Dirac material so that such a topological kink state is achievable and controllable by the same

method employed in bilayer graphene. The studied model can serve as a method to generate the pure valley K or K' current in one electrode and more importantly, this can be controlled in a nonlocal way.

4. Conclusion

In summary, we have investigated the possible topological kink state in the α-T_3 lattice employed to obtain fully polarized nonlocal VSC in a ring-shaped structure. We present the transport calculations and show that the nonlocal VSC is spatially separated from the electron cotunneling. The fully polarized nonlocal VSC can be manipulated by using either a nonlocal gate voltage or the system parameter α, both of them can make nonlocal VSC oscillate periodically due to the quantum interference effect.

Acknowledgments

The work was supported by the National Natural Science Foundation of China (Grant No. 12174051). J. W. also thanks support from the Fundamental Research Funds for the Central Universities.

References

[1] Deutscher G 2005 *Rev. Mod. Phys.* **77** 109
[2] Buzdin A I 2005 *Rev. Mod. Phys.* **77** 935
[3] Beenakker C W J 2008 *Rev. Mod. Phys.* **80** 1337
[4] Beenakker C W J 2006 *Phys. Rev. Lett.* **97** 067007
[5] Linder J and Yokoyama T 2014 *Phys. Rev. B* **89** 020504
[6] Wang J, Hao L and Chan K S 2015 *Phys. Rev. B* **91** 085415
[7] Li H 2016 *Phys. Rev. B* **94** 075428
[8] Zhang Q, Fu D, Wang B, zhang R and Xing D Y 2008 *Phys. Rev. Lett.* **101** 047005
[9] Li W Y, Wu Q P, Liu Z Z, Liu F F and Xiao X B 2023 *J. Appl. Phys.* **133** 143903
[10] Bai C, Yang Y and Zhang X 2008 *Appl. Phys. Lett.* **92** 102513
[11] Beenakker C W J, Gnezdilov N V, Dresselhaus E, Ostroukh V P, Herasymenko Y, Adagideli İ and Tworzydlo J 2018 *Phys. Rev. B* **97** 241403
[12] Martin I, Blanter Y M and Morpurgo A F 2008 *Phys. Rev. Lett.* **100** 036804
[13] Semenoff G W, Semenoff V and Zhou F 2008 *Phys. Rev. Lett.* **101** 087204
[14] Ju L, Shi Z W, Nair N, Lv Y C, Jin C H, Jr J V, Ojeda-Aristizabal C, Bechtel H A, Martin M C, Zettl A, Analytis J and Wang F 2015 *Nature* **520** 650
[15] Yin L J, Jiang H, Qiao J B and He L 2016 *Nat. Commun.* **7** 11760
[16] Lu J, Qiu C, Ye L, Fan X, Ke M, Zhang F and Liu Z 2017 *Nat. Phys.* **13** 369
[17] Wu X X, Meng Y, Tian J X, Huang Y Z, Xiang H, Han D Z and Wen W J 2017 *Nat. Commun.* **8** 1304
[18] Ye L P, Yang Y T, Hang Z H, Qiu C Y and Liu Z Y 2017 *Appl. Phys. Lett.* **111** 251107
[19] Dong J W, Chen X D, Zhu H Y, Wang Y and Zhang X 2017 *Nat. Mater.* **16** 298
[20] Noh J, Huang S, Chen K P and Rechtsman M C 2018 *Phys. Rev. Lett.* **120** 063902
[21] Gao F, Xue H R, Yang Z j, Lai K, Yu Y, Lin X, Chong Y, Shvets G and Zhang B L 2018 *Nat. Phys.* **14** 140
[22] Cheng S G, Liu H, Jiang H, Sun Q F and Xie X C 2018 *Phys. Rev. Lett.* **121** 156801
[23] Urban D F, Bercioux D, Wimmer M and Hausler W 2011 *Phys. Rev. B* **84** 115136
[24] Malcolm J D and Nicol E J 2015 *Phys. Rev. B* **92** 035118
[25] Okamoto S and Xiao D 2018 *J. Phys. Soc. Jpn.* **87** 041006
[26] Vidal J, Mosseri R and Doucot B 1998 *Phys. Rev. Lett.* **81** 5888
[27] Raoux A, Morigi M, Fuchs J N, Piechon F and Montambaux G 2014 *Phys. Rev. Lett.* **112** 026402
[28] Malcolm J D and Nicol E J 2015 *Phys. Rev. B* **92** 035118
[29] Lu W T and Sun Q F 2021 *Phys. Rev. B* **104** 045418
[30] Tan H, Fu P H, Chen Y R, Liu J F, Wang J and Ma Z 2021 *Phys. Rev. B* **103** 195407
[31] Fisher D S and Lee P A 1981 *Phys. Rev. B* **23** 6851
[32] Xu Y, Chen Y R, Wang J, Liu J F and Ma Z 2019 *Phys. Rev. Lett.* **123** 206801
[33] Zhang Z Q, Chen C Z, Wu Y, Jiang H, Liu J, Sun Q F and Xie X C 2021 *Phys. Rev. B* **103** 075434
[34] Ren Y N, Cheng Q, Sun Q F and He L 2022 *Phys. Rev. Lett.* **128** 206805